

A network based approach for unbalanced optimal transport on surfaces

Jiangong Pan¹, Wei Wan², Yuejin Zhang¹, Chenlong Bao^{3,4}, and Zuoqiang Shi^{3,4,*}

¹ *Department of Mathematical Sciences, Tsinghua University, Beijing, 100084, China.*

² *School of Mathematics and Physics, North China Electric Power University, Beijing, China.*

³ *Yau Mathematical Sciences Center, Tsinghua University, Beijing, 100084, China.*

⁴ *Yanqi Lake Beijing Institute of Mathematical Sciences and Applications, Beijing, 101408, China.*

Abstract. In this paper, we present a neural network approach to address the dynamic unbalanced optimal transport problem on surfaces with point cloud representation. For surfaces with point cloud representation, traditional method is difficult to apply due to the difficulty of mesh generating. Neural network is easy to implement even for complicate geometry. Moreover, instead of solving the original dynamic formulation, we consider the Hamiltonian flow approach, i.e. Karush-Kuhn-Tucker system. Based on this approach, we can exploit mathematical structure of the optimal transport to construct the neural network and the loss function can be simplified. Extensive numerical experiments are conducted for surfaces with different geometry. We also test the method for point cloud with noise, which shows stability of this method. This method is also easy to generalize to diverse range of problems.

AMS subject classifications: 65K10, 68T05, 68T07

Key words: unbalanced optimal transport, Hamiltonian flow, point cloud, neural network.

1 Introduction.

The concept of optimal transport (OT) stands as a foundational cornerstone, offering profound insights across numerous domains, including economics, physics, image processing, and machine learning [1]. At its essence, OT is concerned with devising the most efficient means of reallocating resources from source to target allocation points while

*Corresponding author. *Email addresses:* mathpjg@sina.com (J. Pan), weiw@ncepu.edu.cn (W. Wan), zhangyj19@mails.tsinghua.edu.cn (Y. Zhang), clbao@tsinghua.edu.cn (C. Bao), zqshi@tsinghua.edu.cn (Z. Shi)

minimizing associated costs. While the conventional perspective on the OT problem revolves around achieving equilibrium, wherein the total mass of the source distribution aligns precisely with the target distribution, real-world scenarios often disrupt this equilibrium, resulting in resource distributions that introduce disparities in mass. These real-world scenarios have given rise to the development of the unbalanced optimal transport (UOT) problem, an extension designed to address situations characterized by unequal source and target distribution masses [2].

In the unbalanced rendition of the OT problem, the central objective of improving efficiency and minimizing transportation costs remains unwavering. However, the introduction of varying masses introduces an additional layer of complexity, presenting both challenges and avenues for exploration. This multifaceted issue finds applications across a spectrum of fields, including image registration [3–5], transformation and generation [6–8], as well as climate modeling [9–11], style transfer [8,12,13], and medical imaging [14–16]. Despite achieving notable numerical successes, the UOT problem grapples with computational constraints, as diverse conditions often pose formidable challenges for conventional methods, which severely limits the applicability of UOT in different scenarios.

OT problem has three different formulation: Monge problem, Kantorovich problem and Benamou-Brenier problem. In 1781, Monge formulated OT problem as an optimization problem of minimizing the cost functional over all feasible transport plan [17]. However, solving the Monge problem directly has proven to be a formidable task, primarily due to its intricate non-convex nature and the absence of minimal solutions.

To address this challenge, Kantorovich introduce a new formulation by relaxing the transport plan to joint distribution [18]. With this elegant relaxation, OT problem can be formulated as a linear programming problem which can be solved efficiently. Many powerful algorithms have been developed based on Kantorovich formulation, such as Sinkhorn method [1] etc.

Benamou and Brenier [19] made a groundbreaking contribution by introducing the dynamic formulation into the optimal transport problem. Consider the model over a time interval T and a spatial region Ω . Here, ρ represents the density, and v denotes the velocity of the density. In the dynamic OT problem, we are concerned with ρ , subject to given initial and terminal densities ρ_0 and ρ_1 , and (ρ, v) must satisfy the mass conservation law. The primary objective of OT is to minimize the total cost across all feasible pairs of $(\rho, v) \in \mathcal{C}(\rho_0, \rho_1)$. The problem can be formally stated as follows:

$$\mathcal{W}_2(\rho_0, \rho_1) = \min_{(\rho, v) \in \mathcal{C}(\rho_0, \rho_1)} \int_T \int_{\Omega} \frac{1}{2} \rho(t, x) \|v(t, x)\|^2 dx dt, \quad (1.1)$$

where

$$\mathcal{C}(\rho_0, \rho_1) := \{(\rho, v) : \partial_t \rho + \operatorname{div}(\rho v) = 0, \rho(0, x) = \rho_0(x), \rho(1, x) = \rho_1(x)\}. \quad (1.2)$$

It is noteworthy that the resulting PDE predominantly consists of continuity equations, establishing an inherent connection with fluid mechanics. This intrinsic link with fluid

mechanics broadens the range of potential applications, expanding the scope of the problem to encompass areas such as unnormalized OT [20–22] and mean field games [23–25].

Introducing the source term into the continuity equation and modifying the optimization objective to the Wasserstein-Fisher-Rao (WFR) metric eliminates the constraint of mass conservation, thereby leading us to the dynamic UOT problem. In recent years, significant progress has been made in the field of UOT and its related areas. Important contributions include applications in brain pathology analysis (Gerber et al. [26]), multi-species systems (Gallouët et al. [27]), and theoretical insights into gradient flow (Konratyev et al. [28]). Computational progress includes Sato et al.’s UOT algorithm [29], Pham’s [30] Sinkhorn algorithm for entropic regularized UOT, and Séjourné et al.’s [33] accelerated Sinkhorn and Frank-Wolfe solvers. Chapel et al. [31] linked OT to inverse problems, while Bauer et al. [32] connected WFR UOT to shape distances. Recent work by Beier et al. [34] addressed multi-marginal OT, proving the existence of a unique OT plan and extending the Sinkhorn algorithm. These collective efforts demonstrate the increasing importance of UOT in various scientific fields. But none of them can be effectively extended to the point cloud problem, which is the core of this paper.

In this paper, we introduce an innovative neural network approach based on the Hamiltonian flow formulation. Comparing with the dynamic formulation, Hamiltonian flow reveals intrinsic connection between the velocity field and the potential function, which reduce the complexity of the neural networks. And the loss function can be simplified also.

The rest of our paper is organized as follows. In section 2, we give some relevant work on solving UOT problems in recent years. We generalize the UOT problem to obtain the dynamic manifolds UOT problem, and obtain its equivalent form using KKT conditions in Section 3. Next, we discretize the problem and establish the corresponding loss function. Experimental results and implementation details are given in Section 5. Finally, the conclusion of this paper is placed by us in Section 6.

2 Related work.

In recent years, the field of deep learning has showcased extraordinary achievements across a diverse spectrum of computational challenges. These achievements span from tasks like image classification [35–37], speech recognition [38–40], natural language processing [41–43], numerical approximations of PDE [44–46] and the generation of images [47–49]. The success of these applications suggests that we can also use deep learning to solve UOT problems. In 2018, Yang et al. [50] proposed a scalable UOT method, combining it with neural generative models, specifically Generative Adversarial Networks. Moving forward, in 2020, Lee et al. [51] introduced a novel UOT regularizer formulation with linear optimization-variable complexity, effectively addressing challenges in the inverse imaging problem. Building upon these innovations, in 2021, Ma et al. [52] harnessed UOT distance to quantify discrepancies between predicted density maps and

point annotations, highlighting its robustness against spatial perturbations. In the same year, Le et al. [53] employed UOT as a solution to the unbalanced assignment problem in multi-camera tracking, showcasing its versatility. Additionally, Fatras et al. [54] enhanced robustness through a mini-batch strategy and UOT on large-scale datasets, advancing its practicality in 2021. Progressing to 2022, Cao et al. [55] proposed uniPort, a unified single-cell data integration framework, which effectively manages data heterogeneity across datasets using a coupled variational autoencoder and minibatch unbalanced optimal transport. This scalability extends to large-scale datasets, further enhancing its utility. In the same year, Lübeck et al. [6] developed NUBOT, a semi-coupling based formalism addressing mass creation and destruction, along with an algorithmic scheme derived through a cycle-consistent training procedure. Venturing into 2023, Shen and his team [56] introduced UOTSumm, a pioneering framework for long document summarization. Unlike conventional approaches reliant on biased tools like Rouge, UOTSumm adopts UOT principles to directly learn text alignment from summarization data, rendering it adaptable to existing neural abstractive text summarization models. Similarly, De et al. [57] demonstrated the applicability of UOT in object detection in the same year, achieving state-of-the-art results in both average precision and average recall metrics, while also accelerating initial convergence. Furthermore, in 2023, Dan and colleagues [58] presented Uncertainty-Guided Joint UOT, a comprehensive framework addressing feature distribution alignment and uncertainty posed by noisy training samples through a feature uncertainty estimation mechanism and UOT strategy.

3 Dynamic formulation of UOT

First, we briefly review the dynamic formulation of UOT in Euclidean space. Considering a modeling framework that operates over the time interval $[0, 1]$ and a spatial domain denoted as $\Omega \subset \mathbb{R}^d$. Here, $\rho : [0, 1] \times \Omega \rightarrow \mathbb{R}^+$ defines the density distribution of agent across time $t \in [0, 1]$ and space. The velocity field $\mathbf{v} = (v_1, \dots, v_d) : [0, 1] \times \Omega \rightarrow \mathbb{R}^d$ characterizes the agent's strategy (or control) to affect the evolution of this density. Introducing $g : [0, 1] \times \Omega \rightarrow \mathbb{R}$, a scalar field, which captures the mass growth and depletion. The primary goal of the UOT problem is to effectively reduce the combined costs linked to all permissible pairs of (ρ, \mathbf{v}, g) that adhere to the limitations stipulated by $\mathcal{C}(\rho_0, \rho_1)$. This complex undertaking is conceptualized through the WFR metric:

$$\mathcal{W}_{WFR}(\rho_0, \rho_1) = \min_{(\rho, \mathbf{v}, g) \in \mathcal{C}(\rho_0, \rho_1)} \int_0^1 \int_{\Omega} \frac{1}{2} \rho(t, \mathbf{x}) \|\mathbf{v}(t, \mathbf{x})\|^2 + \frac{1}{\eta} \rho(t, \mathbf{x}) g(t, \mathbf{x})^2 d\mathbf{x} dt, \quad (3.1)$$

where

$$\mathcal{C}(\rho_0, \rho_1) := \{(\rho, \mathbf{v}, g) : \partial_t \rho + \text{div}(\rho \mathbf{v}) = \rho g, \rho(0, \mathbf{x}) = \rho_0(\mathbf{x}), \rho(1, \mathbf{x}) = \rho_1(\mathbf{x})\}, \quad (3.2)$$

and η is a source coefficient which can balance transport and creation/destruction of mass. It is not difficult to find that when $g(t, \mathbf{x}) = 0$, problem (3.1) and (3.2) will degenerate into (1.1) and (1.2) respectively.

In this article, we focus on solving dynamic UOT problems on manifolds. Naturally, we need to extend the dynamic UOT to manifolds and call it the dynamic manifolds UOT (MUOT). In recent years, some researchers have also paid attention to this aspect. Lavenant et al. [59] introduced a groundbreaking methodology that involves interpolating between probability distributions on discrete surfaces, leveraging the principles of optimal transport theory. This innovative technique not only maintains the structural integrity of the data but also engenders the development of a Riemannian metric within the domain of probability distributions pertaining to discrete surfaces. Yu et al. [60] have elegantly demonstrated the profound connection between systems of partial differential equations and optimal conditions for correlated variational forms on intricate manifolds. Moreover, they have ingeniously crafted a proximal gradient method tailored for addressing variational mean-field games.

We consider a mathematical model defined over the time interval $[0,1]$, operating within a compact surface $\Gamma \subset \mathbb{R}^3$. In this paper, we focus on closed surfaces, i.e., $\partial\Gamma = \emptyset$. Let $\rho: [0,1] \times \Gamma \rightarrow \mathbb{R}^+$ denote the density of agents as a function of time $t \in [0,1]$. The density values are constrained to the positive real numbers. Additionally, let $v = (v_1, \dots, v_d) \in T(\Gamma): [0,1] \times \Gamma \rightarrow \mathbb{R}^d$ represent the velocity field associated with the density. The velocity field represents the movement of the mass. Here, $g: [0,1] \times \Gamma \rightarrow \mathbb{R}$ represents a scalar field that characterizes the local growth and depletion of mass within the system. Our main focus is on understanding the behavior of (ρ, v, g) given ρ_0 and ρ_1 densities. Then, the dynamic MUOT can be expressed as

$$\mathcal{W}_M(\rho_0, \rho_1) = \min_{(\rho, v, g) \in \mathcal{C}(\rho_0, \rho_1)} \int_0^1 \int_{\Gamma} \frac{1}{2} \rho(t, x) \|v(t, x)\|^2 + \frac{1}{\eta} \rho(t, x) g(t, x)^2 d\sigma dt, \quad (3.3)$$

where

$$\mathcal{C}(\rho_0, \rho_1) := \{(\rho, v, g) : \partial_t \rho + \text{div}_{\Gamma}(\rho v) = \rho g, \rho(0, x) = \rho_0(x), \rho(1, x) = \rho_1(x)\}, \quad (3.4)$$

and η is a source coefficient which can balance transport and creation/destruction of mass. Let \mathbf{n} denote the outward normal vector of the surface Γ , and \mathcal{I} be the identity operator,

$$P(x) = \mathcal{I} - \mathbf{n}(x)\mathbf{n}(x)^T$$

represents the projection operator of the three-dimensional vector at node x of the manifolds to its tangent component, and the tangential gradient operator, tangential divergence operator at node x are respectively defined

$$\nabla_{\Gamma} = P(x)\nabla, \quad \text{div}_{\Gamma} = \text{trace}(\nabla_{\Gamma}).$$

For dynamic optimal transport on \mathbb{R}^d , it is well known that it can be solved by Hamiltonian flow which is actually Karush-Kuhn-Tucker (KKT) conditions of the dynamic optimal transport.

Inspired by the methodologies presented in Benamou's work [19], we can derive the KKT condition of the UOT problem based on the original variable (ρ, v) on manifold.

Theorem 3.1. Suppose $(\hat{\rho}, \hat{v}, \hat{g}, \hat{\phi}, \hat{\phi}_1, \hat{\phi}_2)$ is a saddle point of (3.5),

$$\begin{aligned} L(\rho, v, g, \phi, \phi_1, \phi_2) = & \int_0^1 \int_{\Gamma} \frac{1}{2} \rho(t, x) \|v(t, x)\|^2 + \frac{1}{\eta} \rho(t, x) g(t, x)^2 d\sigma dt \\ & + \int_0^1 \int_{\Gamma} \phi(t, x) [\partial_t \rho(t, x) + \text{div}_{\Gamma}(\rho(t, x) v(t, x)) - \rho(t, x) g(t, x)] d\sigma dt \\ & + \int_{\Gamma} \phi_1(x) (\rho(0, x) - \rho_0(x)) d\sigma + \int_{\Gamma} \phi_2(x) (\rho(1, x) - \rho_1(x)) d\sigma. \end{aligned} \quad (3.5)$$

Then, solution $(\hat{\rho}, \hat{\phi})$ (where $\hat{v} = \nabla_{\Gamma} \hat{\phi}$ and $\hat{g} = \frac{\eta}{2} \hat{\phi}$) of (3.6) is the optimal solution for (3.3) and (3.4). And we refer to (3.6) as dynamic KKT-MUOT:

$$\begin{aligned} \partial_t \rho + \text{div}_{\Gamma}(\rho \nabla_{\Gamma} \phi) &= \frac{\eta}{2} \rho \phi, \quad (t, x) \in (0, 1) \times \Gamma, \\ \partial_t \phi + \frac{1}{2} \|\nabla_{\Gamma} \phi\|^2 &= -\frac{\eta}{4} \phi^2, \quad (t, x) \in [0, 1] \times \Gamma, \\ \rho(0, x) &= \rho_0(x), \quad \rho(1, x) = \rho_1(x), \quad x \in \Gamma. \end{aligned} \quad (3.6)$$

Proof. Performing a simple partition integral over (3.5), we get

$$\begin{aligned} L(\rho, v, g, \phi, \phi_1, \phi_2) = & \int_0^1 \int_{\Gamma} \frac{1}{2} \rho(t, x) \|v(t, x)\|^2 + \frac{1}{\eta} \rho(t, x) g(t, x)^2 d\sigma dt \\ & + \int_{\Gamma} (\phi(1, x) \rho(1, x) - \phi(0, x) \rho(0, x)) d\sigma - \int_0^1 \int_{\Gamma} \partial_t \phi(t, x) \rho(t, x) d\sigma dt \\ & - \int_0^1 \int_{\Gamma} \nabla_{\Gamma} \phi(t, x) \cdot (\rho(t, x) v(t, x)) + \phi(t, x) \rho(t, x) g(t, x) d\sigma dt \\ & + \int_{\Gamma} \phi_1(x) (\rho(0, x) - \rho_0(x)) d\sigma + \int_{\Gamma} \phi_2(x) (\rho(1, x) - \rho_1(x)) d\sigma. \end{aligned} \quad (3.7)$$

Then computing the saddle point of the above equation, we have

$$\begin{aligned} L_{\rho} = 0 & \Rightarrow \partial_t \phi(t, x) + \nabla_{\Gamma} \phi(t, x) \cdot v(t, x) + \phi(t, x) g(t, x) - \frac{1}{2} \|v(t, x)\|^2 - \frac{1}{\eta} g(t, x)^2 = 0, \\ L_v = 0 & \Rightarrow v(t, x) - \nabla_{\Gamma} \phi(t, x) = 0, \\ L_g = 0 & \Rightarrow \frac{2}{\eta} g(t, x) - \phi(t, x) = 0. \end{aligned} \quad (3.8)$$

Next, we obtain

$$\partial_t \phi + \frac{1}{2} \|\nabla_{\Gamma} \phi\|^2 + \frac{\eta}{4} \phi^2 = 0, \quad (3.9)$$

with $v = \nabla_{\Gamma} \phi$ and $g = \frac{\eta}{2} \phi$. \square

In the subsequent section, we will introduce the neural network approach to solve (3.6).

4 Neural Network approach

In this paper, we use a fully connected deep neural network (FCDNN) as an approximation function. FCDNN is a type of network in which two adjacent layers of neurons in a network are connected to each other. Like common neural networks, it includes neurons, weights, biases, and activation functions. Through the use of known data, the weights and biases are constantly trained to obtain the optimal approximation function. Now let's use FCDNN to approximate ρ, ϕ :

$$\begin{aligned}\rho(t, \mathbf{x}) &= \rho_{NN}(t, \mathbf{x}; \theta) = \mathcal{N}_M \mathcal{N}_{M-1} \mathcal{N}_{M-2} \cdots \mathcal{N}_1 \mathcal{N}_0(\mathbf{x}), \\ \phi(t, \mathbf{x}) &= \phi_{NN}(t, \mathbf{x}; \zeta) = \mathcal{N}_M \mathcal{N}_{M-1} \mathcal{N}_{M-2} \cdots \mathcal{N}_1 \mathcal{N}_0(\mathbf{x}),\end{aligned}\quad (4.1)$$

where \mathbf{x} is the Cartesian coordinate, M is the number of layers of the neural network and $M > 0$ and

$$\begin{cases} \mathcal{N}_0(\mathbf{x}) = \mathbf{x}, \\ \mathcal{N}_m(\mathbf{x}) = \sigma(W_m \mathcal{N}_{m-1}(\mathbf{x}) + b_m), \quad \text{for } 1 \leq m \leq M-1, \\ \mathcal{N}_M(\mathbf{x}) = W_M \mathcal{N}_{M-1}(\mathbf{x}) + b_M. \end{cases}\quad (4.2)$$

$W_m, b_m (1 \leq m \leq M)$ are parameters to be trained. And σ is given activation function. In the subsequent numerical experiments, we use

$$\sigma(\mathbf{x}) = \tanh(\mathbf{x})$$

for ϕ_{NN} . To ensure that the ρ is non-negative, we use the Softplus function

$$\sigma(\mathbf{x}) = \log(1 + e^{\mathbf{x}})$$

in the output layer of $\rho_{NN}(t, \mathbf{x}; \theta)$.

The surface is given by point cloud $\{\mathbf{x}_j\}_{j=1}^N$. Moreover, we assume the associate out normal $\{\mathbf{n}_j\}_{j=1}^N$ is also given. In addition, we need to discretize time by $0 = t^0 < t^1 < \cdots < t^{n-1} < t^n < \cdots < t^{N_t} = T$.

With the approximation of FCDNN to ρ and ϕ , then we need to consider how to update the parameter. Before using the optimization algorithm, we need to establish the corresponding optimization objective, that is, the loss function (also known as the objective function). For KKT-MUOT problem (3.6), the following loss function is established:

$$\mathcal{L}_{MUOT}(\theta, \zeta) = \lambda_c \mathcal{L}_c(\theta, \zeta) + \lambda_{hj} \mathcal{L}_{hj}(\zeta) + \lambda_{ic} \mathcal{L}_{ic}(\theta), \quad (4.3)$$

where

$$\begin{aligned}
\mathcal{L}_c(\theta, \zeta) &= \frac{1}{N_c} \sum_{i=1}^{N_c} \|\partial_t \rho(t_i, \mathbf{x}_i; \theta) + \text{div}_\Gamma(\rho(t_i, \mathbf{x}_i; \theta) \nabla_\Gamma \phi(t_i, \mathbf{x}_i; \zeta)) - \frac{\eta}{2} \rho(t_i, \mathbf{x}_i; \theta) \phi(t_i, \mathbf{x}_i; \zeta)\|^2, \\
\mathcal{L}_{hj}(\zeta) &= \frac{1}{N_{hj}} \sum_{i=1}^{N_{hj}} \|\partial_t \phi(t_i, \mathbf{x}_i; \zeta) + \|\nabla_\Gamma \phi(t_i, \mathbf{x}_i; \zeta)\|^2 + \frac{\eta}{4} \phi(t_i, \mathbf{x}_i; \zeta)^2\|^2, \\
\mathcal{L}_{ic}(\theta) &= \frac{1}{N_{ic}} \sum_{i=1}^{N_{ic}} (\|\rho(0, \mathbf{x}_i; \theta) - \rho_0(\mathbf{x}_i)\|^2 + \|\rho(1, \mathbf{x}_i; \theta) - \rho_1(\mathbf{x}_i)\|^2),
\end{aligned} \tag{4.4}$$

where λ_c , λ_{hj} and λ_{ic} are the weighting coefficients for different loss terms; N_c , N_{hj} and N_{ic} are the numbers of data points for different terms. Various differential operators in the loss function can be computationally obtained by automatic differentiation techniques [61]. In this paper, we use the Adam optimizer [62], an adaptive algorithm for gradient-based first-order optimization, to optimize the model parameters.

5 Numerical Experiments

In this section, we perform a total of five arithmetic cases to verify the effectiveness of the proposed algorithm. The calculations are first performed in the most classical Gaussian example in two dimension. Then the source term coefficients in the UOT problem are explored in the case of the UOT problem, considering different degrees of source terms, and their impact on the transport scheme. Next, we consider the UOT problem on manifolds. And we studied the MOT and MUOT problems on various stream forms with different topology. Further, we consider adding different degrees of Gaussian noise to the point cloud to verify the robustness of our algorithm. Finally, three different shape transport experiments were carried out, by calculating between different patterns, in order to obtain the whole transport scheme. In experiment, if Euclidean space is considered, we need the space boundary condition

$$\rho v \cdot \mathbf{n} = 0.$$

5.1 Gaussian Examples

In this section, we perform numerical experiments on classical Gaussian examples and mixed Gaussian examples on two dimension (2D) spaces using the proposed algorithm to verify the effectiveness.

Two classical examples and the corresponding configurations are given in Table 1, where Gaussian density function is

$$\rho_G(\mathbf{x}, \mu, \Sigma) = \frac{1}{(2\pi)^{1/2} |\Sigma|^{1/2}} e^{-\frac{1}{2}(\mathbf{x}-\mu)^T \Sigma^{-1}(\mathbf{x}-\mu)}.$$

The parameters $\lambda_c = \lambda_{hj} = \lambda_{ic} = 1000$ and $\eta = 2$ are used in this test. We use uniform grid to sample 10 points at time t and 900 points in space (coordinate (x, y)).

Table 1: Initial distribution $\rho_0(x)$, target distribution $\rho_1(x)$ for 2D KKT-UOT.

Test	$\rho_0(x)$	$\rho_1(x)$
A	$\rho_G(x, [0.4, 0.4], 0.01 \cdot \mathbf{I})$	$2\rho_G(x, [0.6, 0.6], 0.005 \cdot \mathbf{I})$
B	$\rho_G(x, [0.5, 0.5], 0.005 \cdot \mathbf{I})$	$\rho_G(x, [0.3, 0.3], 0.005 \cdot \mathbf{I}) + \rho_G(x, [0.7, 0.3], 0.005 \cdot \mathbf{I})$ $+ \rho_G(x, [0.7, 0.7], 0.005 \cdot \mathbf{I}) + \rho_G(x, [0.3, 0.7], 0.005 \cdot \mathbf{I})$

As shown in Figures 1, our method performs well in simple Gaussian translations. In the mixed Gaussian splitting, KKT-OT can also divide as expected.

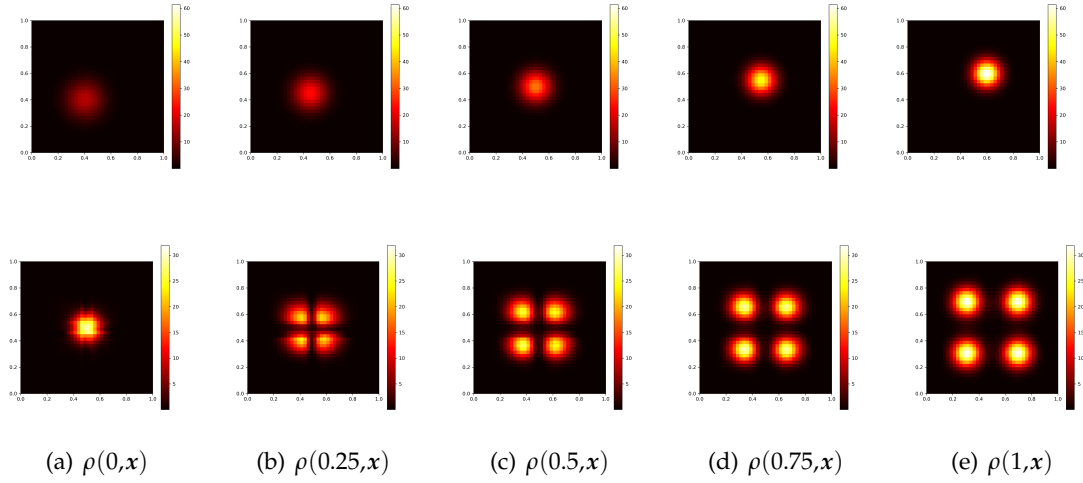


Figure 1: 2D KKT-UOT test. First row: Simple gaussian transport. Second row: Mixed gaussian split transport.

In addition, we give the values of the residuals of the equations in each loss function for Gaussian examples in Table 2. By observing the experimental results, we can know that for simple types of Gaussian shift problems, the residuals of the equations are very small, which means that our algorithm performs very well. But in test B, loss is relatively high since test B is more complicated than test A.

Table 2: Loss value for Gaussian examples.

Test	KKT-OT		
	\mathcal{L}_c	\mathcal{L}_{hj}	\mathcal{L}_{ic}
A	1.50e-2	6.89e-3	5.16e-3
B	3.43e-2	5.46e-2	3.06e-2

In UOT problem (3.1), there is a parameter η . This coefficient controls the creation

or destruction of mass during transport. When $\eta \rightarrow 0$, the UOT solution is supposed to converge to the OT solution. When $\eta \rightarrow \infty$, there should be no transportation at all. In next example, we will investigate effect of η .

In Test C, we set the parameters $\lambda_c = \lambda_{hj} = 100$, $\lambda_{ic} = 1000$. We select different η to test, $\eta = 10^2, 1, 10^{-6}$. The configurations of ρ_0 and ρ_1 are in Table 3. We also use uniform grid to sample 10 points at time t and 800 points in space (coordinate x).

Table 3: UOT with Variable Coefficients.

Test	$\rho_0(x)$	$\rho_1(x)$
C	$\rho_G(x, 0.7, 0.005)$	$0.3\rho_G(x, 0.7, 0.005) + 0.7\rho_G(x, 1.3, 0.005)$

The results for different η are shown in Figure 2 and the results fit the expectation very well. When η is large, the algorithm chooses generation over transport. When η is equal to 1, generation and transport are balanced at this point, matching the experimental phenomenon. When η is small, the algorithm prefers transport and almost no generation and the result almost reduce to OT. The study of different η shows that our algorithm is effective in computing UOT problems with different generation and transport requirements.

5.2 OT on point cloud

In this section, we compute the UOT problems on point cloud. We consider both OT problem $g(t, x) = 0$ and the general UOT problem $g(t, x) \neq 0$.

First, we consider the OT problems on simple manifolds as follows:

- *Sphere*:

$$(x - \frac{1}{2})^2 + (y - \frac{1}{2})^2 + (z - \frac{1}{2})^2 = \frac{1}{4}.$$

- *Ellipsoid*:

$$(x - \frac{1}{2})^2 + 3(y - \frac{1}{2})^2 + 6(z - \frac{1}{2})^2 = \frac{1}{4}.$$

- *Peanut*:

$$\left((4(x - \frac{1}{2}) - 1)^2 + 8(y - \frac{1}{2})^2 + 8(z - \frac{1}{2})^2 \right) \left((4(x - \frac{1}{2}) + 1)^2 + 8(y - \frac{1}{2})^2 + 8(z - \frac{1}{2})^2 \right) = \frac{6}{5}.$$

- *Torus*:

$$\left(0.3 - \sqrt{(x - \frac{1}{2})^2 + (y - \frac{1}{2})^2} \right)^2 + (z - \frac{1}{2})^2 = \frac{1}{25}.$$

- *Opener*:

$$\left(3(x - \frac{1}{2})^2 (1 - 5(x - \frac{1}{2})^2) - 5(y - \frac{1}{2})^2 \right)^2 + 5(z - \frac{1}{2})^2 = \frac{1}{60}.$$

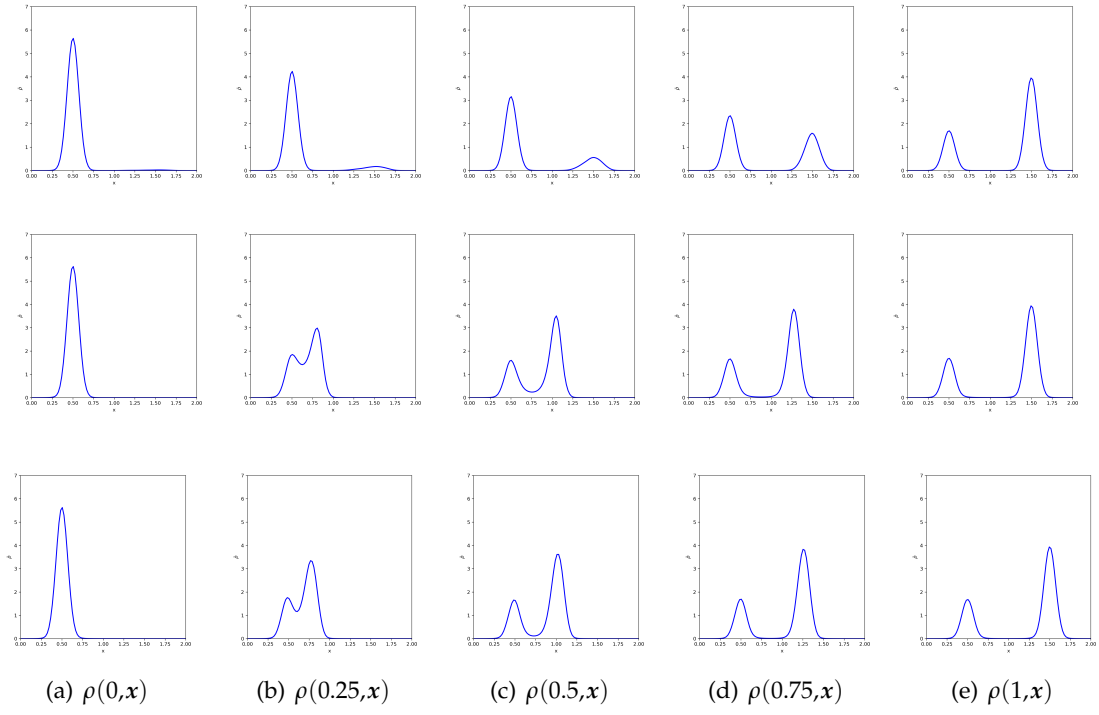


Figure 2: Variable Coefficients UOT: Numerical results for different η , from top to bottom each line $\eta = 10^2, 1, 10^{-6}$.

As can be found in Table 4, we give the settings of the initial distribution $\rho_0(\mathbf{x})$ and the terminating distribution $\rho_1(\mathbf{x})$ on different manifolds, where Gaussian density function on manifolds in [63] is defined as

$$\hat{\rho}_G(\mathbf{x}, \mu, \sigma) = ce^{-\frac{\|\mu - \mathbf{x}\|^2}{\sigma}},$$

and c is a constant. In this article, we consider $c = 100$. In addition to this, we choose $\lambda_c = \lambda_{hj} = 1$, $\lambda_{ic} = 1000$. And we use uniform point picking to sample 10 points at time t , isosurface method to sample 1158, 1222, 1430, 2120 and 1410 points on each surface (coordinate (x, y, z)). Isosurface method is to generate a large number of mesh nodes according to uniform sampling in three-dimensional space. Then calculate isosurface according to surface expression. And finally extract surface nodes.

Table 4: Initial distribution $\rho_0(\mathbf{x})$, target distribution $\rho_1(\mathbf{x})$ for MOT testing.

Test	$\rho_0(\mathbf{x})$	$\rho_1(\mathbf{x})$
Sphere	$\hat{\rho}_G(\mathbf{x}, [0.5, 0.5, 0], 0.01 \cdot \mathbf{I})$	$\hat{\rho}_G(\mathbf{x}, [0.5, 0.5, 1], 0.01 \cdot \mathbf{I})$
Ellipsoid	$\hat{\rho}_G(\mathbf{x}, [0.5, 0.5, \frac{6+\sqrt{6}}{12}], 0.01 \cdot \mathbf{I})$	$\hat{\rho}_G(\mathbf{x}, [0.5, 0.5, \frac{6-\sqrt{6}}{12}], 0.01 \cdot \mathbf{I})$
Peanut	$\hat{\rho}_G(\mathbf{x}, [\frac{2+\sqrt{1+\sqrt{\frac{6}{5}}}}{4}, 0.5, 0.5], 0.01 \cdot \mathbf{I})$	$\hat{\rho}_G(\mathbf{x}, [\frac{2+\sqrt{1-\sqrt{\frac{6}{5}}}}{4}, 0.5, 0.5], 0.01 \cdot \mathbf{I})$
Torus	$\hat{\rho}_G(\mathbf{x}, [\frac{5+4\sqrt{\frac{1}{2}}}{10}, \frac{5+4\sqrt{\frac{1}{2}}}{10}, 0.5], 0.01 \cdot \mathbf{I})$	$\hat{\rho}_G(\mathbf{x}, [\frac{5-4\sqrt{\frac{1}{2}}}{10}, \frac{5-4\sqrt{\frac{1}{2}}}{10}, 0.5], 0.01 \cdot \mathbf{I})$
Opener	$\hat{\rho}_G(\mathbf{x}, [\frac{1+\sqrt{\frac{1+2\sqrt{\frac{1}{15}}}}{10}}{2}, 0.5, 0.5], 0.01 \cdot \mathbf{I})$	$\hat{\rho}_G(\mathbf{x}, [0.5, \frac{1-\sqrt{\frac{1+2\sqrt{\frac{1}{15}}}}{10}}{2}, 0.5], 0.01 \cdot \mathbf{I})$

The results are shown in Figures 3. In these cases, the ground truth is not known, so we can not compare the numerical solutions with the exact ones. However, the neural network based method still is capable to capture the phenomena that the mass is transported along the geodesics, which suggest that our method captures the main character of the solution. The loss given in Table 7 also verifies the effectiveness of our method.

Further, we test the Gaussian distribution and mixed Gaussian distribution OT problems on a 2D sphere embedded in four-dimensional space. We directly add a new dimension to the sampled sphere point in three-dimensional and assign it to 0, that is, $(x, y, z, w) = (x, y, z, 0)$. Then the zOw plane is rotated by M_R :

$$M_R = \begin{pmatrix} 1 & 0 & 0 & 0 \\ 0 & 1 & 0 & 0 \\ 0 & 0 & \frac{\sqrt{2}}{2} & -\frac{\sqrt{2}}{2} \\ 0 & 0 & \frac{\sqrt{2}}{2} & \frac{\sqrt{2}}{2} \end{pmatrix}.$$

Then, the point cloud is obtained. In this experiment, we used the parameter $\lambda_c = \lambda_{hj} = 10$, $\lambda_{ic} = 1000$. In Table 5, we give the settings of the initial distribution $\rho_0(\mathbf{x})$ and the terminating distribution $\rho_1(\mathbf{x})$ in four-dimensional space.

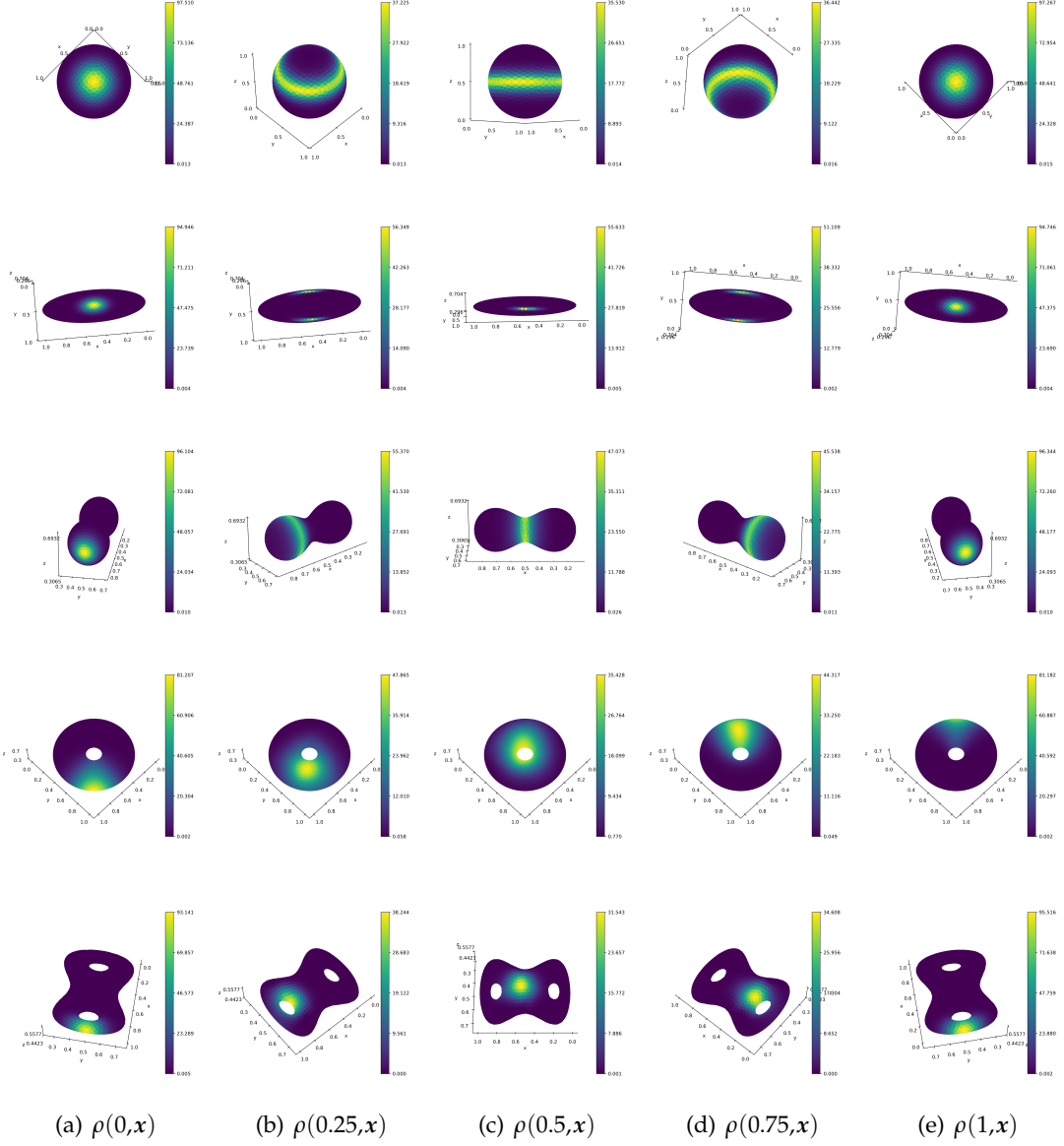


Figure 3: OT tests on point cloud.

Table 5: Initial distribution $\rho_0(x)$, target distribution $\rho_1(x)$ for MOT testing in four-dimensional space.

Test	$\rho_0(x)$	$\rho_1(x)$
S-G4	$\hat{\rho}_G(x, [0.5, 0.5, \frac{\sqrt{2}}{2}, \frac{\sqrt{2}}{2}], 0.05 \cdot \mathbf{I})$	$\hat{\rho}_G(x, [0.5, 0.5, 0, 0], 0.05 \cdot \mathbf{I})$
S-MG4	$\hat{\rho}_G(x, [0.5, 0.5, \frac{\sqrt{2}}{2}, \frac{\sqrt{2}}{2}], 0.05 \cdot \mathbf{I})$	$\hat{\rho}_G(x, [\frac{1+i}{2}, \frac{1+j}{2}, \frac{\sqrt{2}}{4}, \frac{\sqrt{2}}{4}], 0.05 \cdot \mathbf{I}), (i + j) = 1, i, j \in \mathbb{Z}$

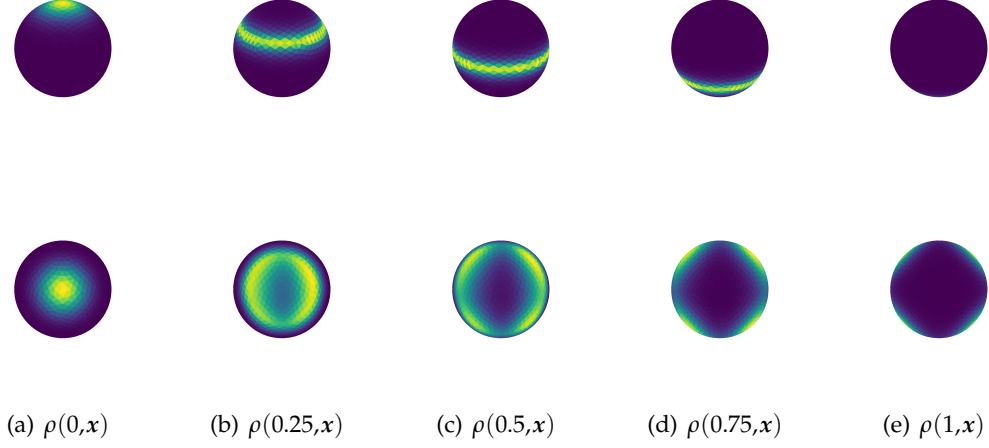


Figure 4: OT tests on point cloud in four-dimensional space.

As shown in Figures 4, our method can still capture the mass transport trajectory in higher dimensional space. The losses given in Table 7 also verify the validity of our method.

5.3 UOT on point cloud

With the success of the MOT described above, we next turn our attention to the MUOT. The mixed Gaussian UOT problem on the *sphere* is taken as our main object of study. We set the configuration of $\rho_0(\mathbf{x})$ and $\rho_1(\mathbf{x})$ in Table 6. And we use uniform point picking to sample 10 points at time t , isosurface method to sample 1158 points on Sphere (coordinate (x, y, z)). The main parameters are set by us to $\eta = 2$ and $\lambda_c = \lambda_{hj} = 1$, $\lambda_{ic} = 1000$. Also back to the mixed Gaussian function as:

$$\begin{aligned} \rho_{MG}(\mathbf{x}) = & \frac{1}{2} \hat{\rho}_G(\mathbf{x}, [0.5, 0, 0.5], 0.01 \cdot \mathbf{I}) + \frac{1}{2} \hat{\rho}_G(\mathbf{x}, [0.5, 1, 0.5], 0.01 \cdot \mathbf{I}) \\ & + \frac{1}{2} \hat{\rho}_G(\mathbf{x}, [0, 0.5, 0.5], 0.01 \cdot \mathbf{I}) + \frac{1}{2} \hat{\rho}_G(\mathbf{x}, [1, 0.5, 0.5], 0.01 \cdot \mathbf{I}). \end{aligned} \quad (5.1)$$

Table 6: Initial distribution $\rho_0(\mathbf{x})$, target distribution $\rho_1(\mathbf{x})$ for MUOT testing.

Test	$\rho_0(\mathbf{x})$	$\rho_1(\mathbf{x})$
M1	$\rho_{MG}(\mathbf{x})$	$\hat{\rho}_G(\mathbf{x}, [0.5, 0.5, 1.0], 0.01 \cdot \mathbf{I})$
M2	$\hat{\rho}_G(\mathbf{x}, [0.5, 0.5, 1.0], 0.01 \cdot \mathbf{I})$	$\rho_{MG}(\mathbf{x})$

In Figure 5, we give two different examples for the merging and splitting of mixed Gaussian. The initial and terminal distribution have different mass, unbalanced optimal

transport is still capable to match two distributions due to the help of the mass generation term. However, in Figure 5, merging and splitting process are not exact symmetric which means that the training of neural network may be stacked in a local minimum. Furthermore, here we are considering the imbalance problem, in the process of mass merging (M1) and splitting (M2), the increase and decrease of mass is controlled by the source term ρg in the equation (3.4).

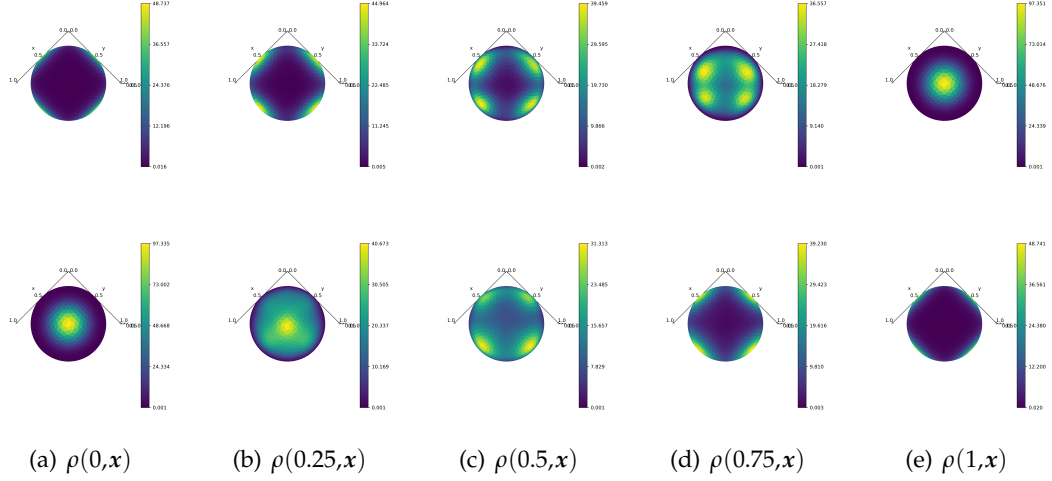


Figure 5: MUOT test on Sphere.

In addition, we give the values of the residuals of the equations for each loss function in all manifolds instances in Table 7. In our experiments, we set the stopping threshold, $\delta < 0.1$ or the number of iterations is less than 20000. In all cases, the residual reduce to a small level. However, for complicate surfaces, the residual may be relatively higher, especially for the residual of the continuous equation.

5.4 Noisy Manifolds

Now, we consider adding Gaussian noise to the point cloud to test the robustness of our algorithm. First, we add Gaussian noise to normals. The variance of noise is $\omega_n \sigma_n$ and σ_n is the variance of the normals. The perturbed normals are given in Figure 6. The associate results are shown in Figure 7. When noise level is 1% and 5%, the transport phenomenon can still be captured. But when the noise is greater than 10%, our algorithm cannot continue to maintain this success.

The method is more sensitive to the perturbation on points. As shown in Figure 9, 5% noise is enough to make the method fail to give the true solution.

Finally, we add noise to both points and normal vectors, Figure 11. In this case, the performance is similar to points perturbed only case, only with 1% noise, the result is

Table 7: Loss value for all Manifold examples.

Test	Manifold Examples			
	\mathcal{W}_M	\mathcal{L}_c	\mathcal{L}_{hj}	\mathcal{L}_{ic}
Sphere	1.40e1	9.93e-2	6.98e-2	3.87e-3
Ellipsoid	4.75e0	4.76e-1	9.35e-2	1.31e-3
Peanut	1.42e0	2.98e-1	8.64e-2	2.21e-2
Torus	8.82e0	1.21e-1	6.48e-2	1.06e-3
Opener	1.22e0	2.95e-1	8.62e-2	1.81e-3
M1	8.97e0	1.09e-1	8.21e-3	5.82e-4
M2	1.08e1	9.98e-2	7.70e-3	4.64e-4
S-G4	1.22e1	9.76e-2	3.66e-2	2.21e-2
S-MG4	5.91e0	9.98e-2	1.00e-2	1.22e-2

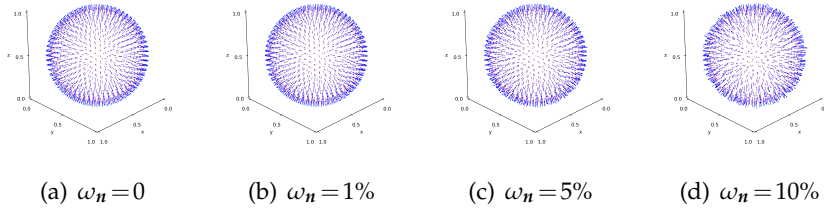


Figure 6: Normal vector with different level of noise.

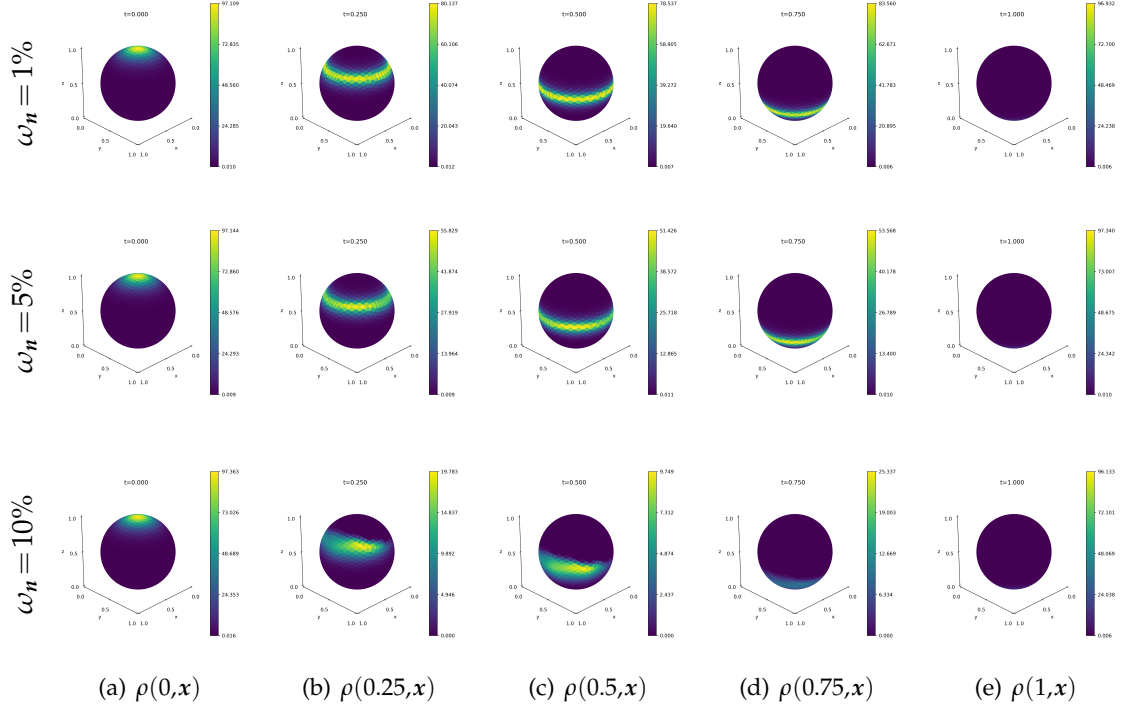


Figure 7: MOT test on sphere with different noise on normal vector.

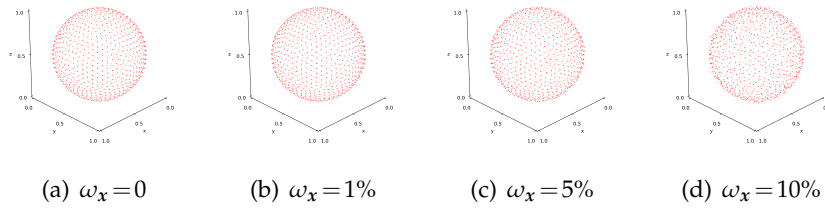


Figure 8: point cloud with different level of noise.

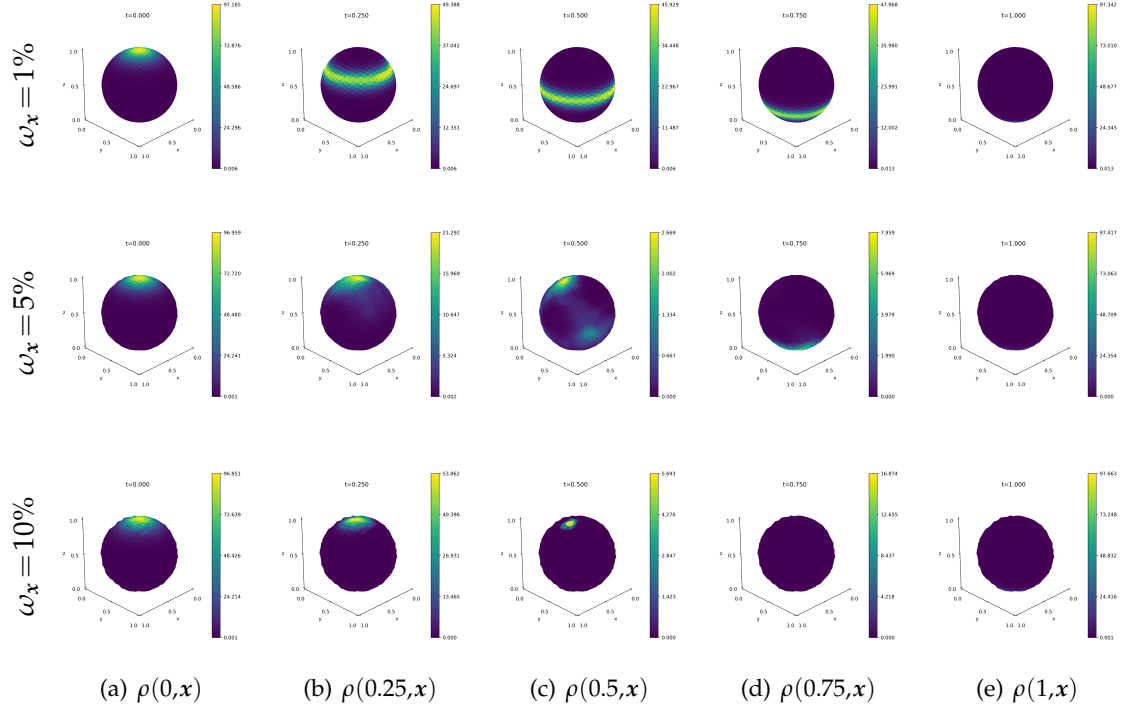


Figure 9: MOT test on sphere with different noise on point cloud.

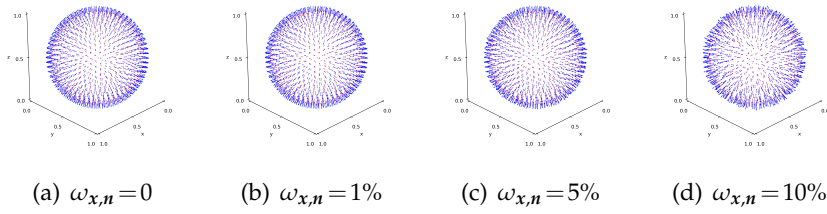


Figure 10: points and normal vector with different level of noise added to the sphere.

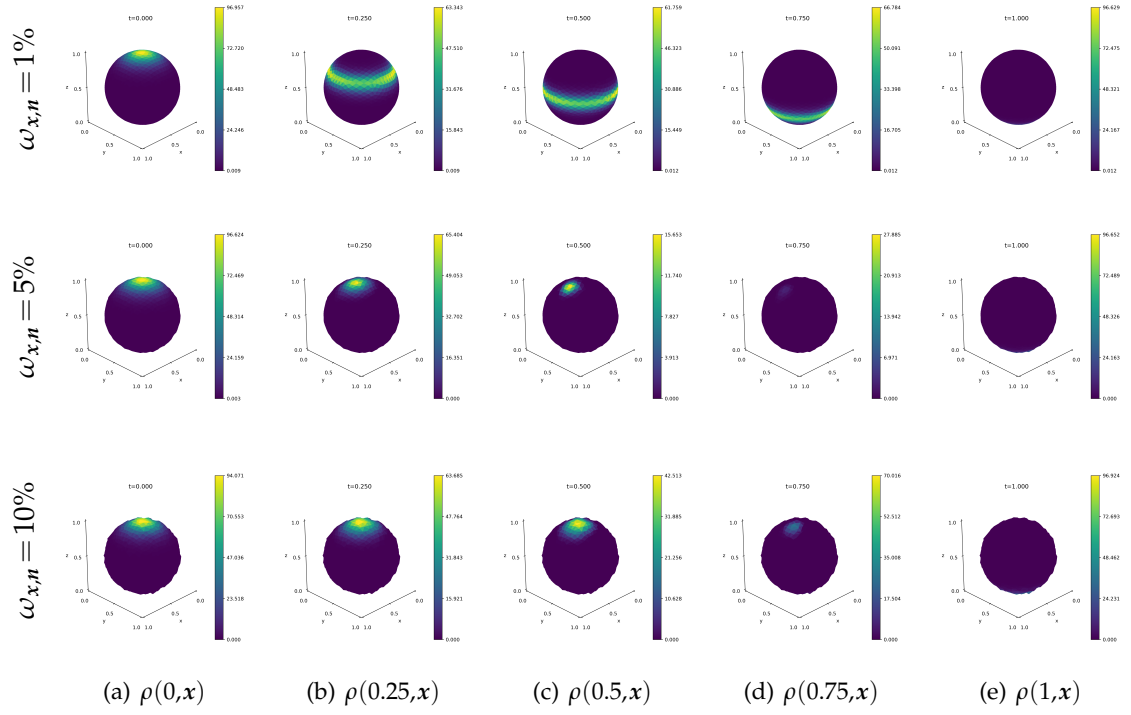


Figure 11: MOT test on sphere with different noise on both points and normal vectors.

stable. Finally, we give the value of loss function in Table 8. With different noise level,

Table 8: Loss value for different noise on sphere.

		1%	5%	10%
ω_n	\mathcal{W}_M	2.48e1	1.55e1	5.48e0
	\mathcal{L}_c	3.67e0	5.43e0	2.29e0
	\mathcal{L}_{hj}	7.29e-1	2.37e-1	7.49e-1
	\mathcal{L}_{ic}	4.81e-3	2.46e-3	1.67e-2
ω_x	\mathcal{W}_M	1.56e1	1.43e0	1.09e0
	\mathcal{L}_c	5.40e-1	9.87e-1	1.80e-1
	\mathcal{L}_{hj}	1.94e-1	8.82e-2	2.06e-2
	\mathcal{L}_{ic}	1.99e-2	2.05e-2	5.51e-3
$\omega_{x,n}$	\mathcal{W}_M	1.94e1	1.43e0	7.11e-1
	\mathcal{L}_c	4.30e0	1.05e0	2.10e0
	\mathcal{L}_{hj}	3.55e-1	1.69e-1	8.24e-2
	\mathcal{L}_{ic}	8.05e-2	2.95e-2	1.59e-2

1%, 5%, 10%, the loss is comparable. But the results are completely change in high noise cases, due to the perturbation of points and normal vectors.

5.5 Shape Transfer

Finally, we apply our method on shape transfer problem. In shape transfer problem, the initial and terminal shape may have different mass, so unbalanced optimal transport provide a good model for this problem. We give three examples of shape transfer in Figure 12. All images are 28×28 in size. In our experiments, we choose the imbalance parameter $\eta = 2$, $\lambda_c = \lambda_{hj} = \lambda_{ic} = 1000$. And we use uniform point picking to sample 10 points at time t and 784 points on space (coordinate (x, y)).

For the first shape transfer example, the initial shape is a disc and we want to transfer it to a hexagram, as shown in the first row of Figure 12. In the second row, we show the result of transferring a triangle to a smiley face. The last example is the transfer between digit numbers which are extracted from MNIST dataset. In all tests, our method gives reasonable results to transfer shapes which demonstrate the effectiveness of the proposed method.

6 Conclusion

We propose a neural network-based method to solve UOT problem on point cloud. This method has good versatility and can save computational costs while avoiding mesh generation. Numerical experiments show that our method can effectively deal with MUOT problem. In current algorithm, the out normals of point cloud is also required. In the

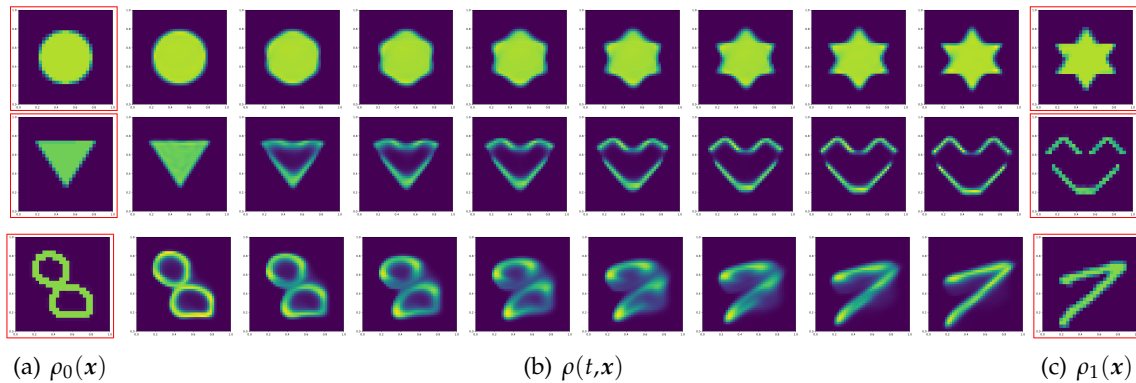


Figure 12: Shape transfer at different moments.

subsequent work, we will study the numerical method without explicitly given out normals.

Acknowledgments

This work is supported by National Natural Science Foundation of China (NSFC) No. 92370125 and No. 12301538 and the National Key R&D Program of China No. 2021YFA1001300.

References

- [1] C. Villani, Topics in optimal transportation, volume 58, American Mathematical Soc., 2021.
- [2] T. Séjourné, G. Peyré and F. X. Vialard, Unbalanced optimal transport, from theory to numerics, Handbook of Numerical Analysis, 24:407–471, 2023.
- [3] J. Feydy, B. Charlier, F. X. Vialard and G. Peyré, Optimal transport for diffeomorphic registration, In Medical Image Computing and Computer Assisted Intervention-MICCAI 2017: 20th International Conference, Quebec City, QC, Canada, September 11-13, 2017, Proceedings, Part I 20, pages 291–299, Springer, 2017.
- [4] H. X. Qin, Y. C. Zhang, Z. T. Liu and B. C. Chen, Rigid registration of point clouds based on partial optimal transport. In Computer Graphics Forum, volume 41, 6, pages 365–378, Wiley Online Library, 2022.
- [5] N. Bonneel and J. Digne, A survey of optimal transport for computer graphics and computer vision. In Computer Graphics Forum, volume 42, 2, pages 439–460, Wiley Online Library, 2023.
- [6] F. Lücke, C. Bunne, G. Gut, J. S. D. Castillo, L. Pelkmans and D. Alvarez-Melis, Neural unbalanced optimal transport via cycle-consistent semi-couplings, In NeurIPS 2022 AI for Science: Progress and Promises, 2022.
- [7] Y. M. Chen, Y. Y. Lan, R. B. Xiong, L. Pang, Z. M. Ma and X. Q. Cheng, Evaluating natural language generation via unbalanced optimal transport, In Proceedings of the Twenty-Ninth

- International Conference on International Joint Conferences on Artificial Intelligence, pages 3730–3736, 2021.
- [8] J. Li, L. W. Wu, D. Xu and S. W. Yao, Arbitrary style transfer with attentional networks via unbalanced optimal transport, *IET Image Processing*, 16(7):1778–1792, 2022.
 - [9] G. Vissio, V. Lembo, V. Lucarini and M. Ghil, Evaluating the performance of climate models based on wasserstein distance, *Geophysical Research Letters*, 47(21):e2020GL089385, 2020.
 - [10] T. Sun, B. Liu, T. Hasegawa, Z. Y. Liao, L. Tang, L. L. Liu, W. X. Cao and Y. Zhu, Sink-source unbalance leads to abnormal partitioning of biomass and nitrogen in rice under extreme heat stress: An experimental and modeling study, *European Journal of Agronomy*, 142:126678, 2023.
 - [11] G. Reiersen, D. Dao, B. Björn, K. Klemmer, K. Amara, A. Steinegger, C. Zhang and X. X. Zhu, Reforestree: A dataset for estimating tropical forest carbon stock with deep learning and aerial imagery, In *Proceedings of the AAAI Conference on Artificial Intelligence*, volume 36, 11, pages 12119–12125, 2022.
 - [12] Hao Zhu, Chaoyou Fu, Qianyi Wu, Wayne Wu, Chen Qian and Ran He, Aot: Appearance optimal transport based identity swapping for forgery detection, *Advances in Neural Information Processing Systems*, 33:21699–21712, 2020.
 - [13] J. Li, D. Xu and S. W. Yao, Sliced wasserstein distance for neural style transfer, *Computers & Graphics*, 102:89–98, 2022.
 - [14] J. Feydy, P. Roussillon, Alain Trouvé and Pietro Gori, Fast and scalable optimal transport for brain tractograms, In *Medical Image Computing and Computer Assisted Intervention—MICCAI 2019: 22nd International Conference, Shenzhen, China, October 13–17, 2019, Proceedings, Part III* 22, pages 636–644, Springer, 2019.
 - [15] J. Feydy and A. Trouvé. Global divergences between measures: from hausdorff distance to optimal transport, In *International Workshop on Shape in Medical Imaging*, pages 102–115, Springer, 2018.
 - [16] S. Gerber, M. Niethammer, E. Ebrahim, J. Piven, S. R. Dager, M. Styner, S. Aylward and A. Enquobahrie, Optimal transport features for morphometric population analysis, *Medical Image Analysis*, 84:102696, 2023.
 - [17] G. Monge, Mémoire sur la théorie des déblais et des remblais, *Mem. Math. Phys. Acad. Royale Sci.*, pages 666–704, 1781.
 - [18] L. V. Kantorovich, On the translocation of masses, *Journal of mathematical sciences*, 133(4):1381–1382, 2006.
 - [19] J. D. Benamou and Y. Brenier, A computational fluid mechanics solution to the monge-kantorovich mass transfer problem, *Numerische Mathematik*, 84(3):375–393, 2000.
 - [20] W. Gangbo, W. C. Li, S. Osher and M. Puthawala, Unnormalized optimal transport, *Journal of Computational Physics*, 399:108940, 2019.
 - [21] W. J. Lee, R. J. Lai, W. C. Li and S. Osher, Generalized unnormalized optimal transport and its fast algorithms, *Journal of Computational Physics*, 436:110041, 2021.
 - [22] W. J. Lee, R. J. Lai, W. C. Li and S. Osher, Fast algorithms for generalized unnormalized optimal transport, 2019.
 - [23] J. M. Lasry and P. L. Lions, Mean field games, *Japanese journal of mathematics*, 2(1):229–260, 2007.
 - [24] A. Bensoussan, J. Frehse, Phillip Yam, *Mean field games and mean field type control theory*, volume 101, Springer, 2013.
 - [25] R. Carmona, F. Delarue, *Probabilistic theory of mean field games with applications I-II*, Springer, 2018.

- [26] S. Gerber, M. Niethammer, M. Styner and S. Aylward, Exploratory population analysis with unbalanced optimal transport, In Medical Image Computing and Computer Assisted Intervention–MICCAI 2018: 21st International Conference, Granada, Spain, September 16-20, 2018, Proceedings, Part III 11, pages 464–472, Springer, 2018.
- [27] T. Gallouët, M. Laborde and L. Monsaingeon, An unbalanced optimal transport splitting scheme for general advection-reaction-diffusion problems, *ESAIM: Control, Optimisation and Calculus of Variations*, 25:8, 2019.
- [28] S. Kondratyev and D. Vorotnikov, Convex sobolev inequalities related to unbalanced optimal transport, *Journal of Differential Equations*, 268(7):3705–3724, 2020.
- [29] R. Sato, M. Yamada and H. Kashima, Fast unbalanced optimal transport on a tree, *Advances in neural information processing systems*, 33:19039–19051, 2020.
- [30] K. Pham, K. Le, N. Ho, T. Pham and H. Bui, On unbalanced optimal transport: An analysis of sinkhorn algorithm, In International Conference on Machine Learning, pages 7673–7682, PMLR, 2020.
- [31] L. Chapel, R. Flamary, H. R. Wu, C. Févotte and G. Gasso, Unbalanced optimal transport through non-negative penalized linear regression, *Advances in Neural Information Processing Systems*, 34:23270–23282, 2021.
- [32] M. Bauer, E. Hartman and E. Klassen, The square root normal field distance and unbalanced optimal transport, *Applied Mathematics & Optimization*, 85(3):35, 2022.
- [33] T. Séjourné, F. X. Vialard and G. Peyré, Faster unbalanced optimal transport: Translation invariant sinkhorn and 1-d frank-wolfe, In International Conference on Artificial Intelligence and Statistics, pages 4995–5021, PMLR, 2022.
- [34] F. Beier, J. V. Lindheim, S. Neumayer and G. Steidl, Unbalanced multi-marginal optimal transport, *Journal of Mathematical Imaging and Vision*, 65(3):394–413, 2023.
- [35] F. Wang, M. Q. Jiang, C. Qian, S. Yang, C. Li, H. G. Zhang, X. G. Wang and X. O. Tang, Residual attention network for image classification, In Proceedings of the IEEE conference on computer vision and pattern recognition, pages 3156–3164, 2017.
- [36] W. Rawat and Z. H. Wang, Deep convolutional neural networks for image classification: A comprehensive review, *Neural computation*, 29(9):2352–2449, 2017.
- [37] D. S. Lu and Q. H. Weng, A survey of image classification methods and techniques for improving classification performance, *International journal of Remote sensing*, 28(5):823–870, 2007.
- [38] W. Chan, N. Jaitly, Q. Le and O. Vinyals, Listen, attend and spell: A neural network for large vocabulary conversational speech recognition, In 2016 IEEE international conference on acoustics, speech and signal processing (ICASSP), pages 4960–4964, IEEE, 2016.
- [39] L. Deng, G. Hinton and B. Kingsbury, New types of deep neural network learning for speech recognition and related applications: An overview, In 2013 IEEE international conference on acoustics, speech and signal processing, pages 8599–8603, IEEE, 2013.
- [40] O. Abdel-Hamid, A. R. Mohamed, H. Jiang, L. Deng, G. Penn and D. Yu, Convolutional neural networks for speech recognition, *IEEE/ACM Transactions on audio, speech and language processing*, 22(10):1533–1545, 2014.
- [41] Y. Goldberg, A primer on neural network models for natural language processing, *Journal of Artificial Intelligence Research*, 57:345–420, 2016.
- [42] Y. Goldberg, *Neural network methods for natural language processing*, Springer Nature, 2022.
- [43] R. Collobert and J. Weston, A unified architecture for natural language processing: Deep neural networks with multitask learning, In Proceedings of the 25th international conference

- on Machine learning, pages 160–167, 2008.
- [44] Y. H. Zang, G. Bao, X. J. Ye and H. M. Zhou, Weak adversarial networks for high-dimensional partial differential equations, *Journal of Computational Physics*, 411:109409, 2020.
 - [45] B. Yu, The deep ritz method: a deep learning-based numerical algorithm for solving variational problems, *Communications in Mathematics and Statistics*, 6(1):1–12, 2018.
 - [46] M. Raissi, P. Perdikaris and G. E. Karniadakis, Physics-informed neural networks: A deep learning framework for solving forward and inverse problems involving nonlinear partial differential equations, *Journal of Computational physics*, 378:686–707, 2019.
 - [47] H. Q. Fan, H. Su and L. J. Guibas, A point set generation network for 3d object reconstruction from a single image, In *Proceedings of the IEEE conference on computer vision and pattern recognition*, pages 605–613, 2017.
 - [48] K. Gregor, I. Danihelka, A. Graves, D. Rezende and D. Wierstra, Draw: A recurrent neural network for image generation, In *International conference on machine learning*, pages 1462–1471, PMLR, 2015.
 - [49] Y. Taigman, A. Polyak and L. Wolf, Unsupervised cross-domain image generation, *arXiv preprint arXiv:1611.02200*, 2016.
 - [50] K. D. Yang and C. Uhler, Scalable unbalanced optimal transport using generative adversarial networks, In *International Conference on Learning Representations*, 2018.
 - [51] J. Lee, N. P. Bertrand and C. J. Rozell, Unbalanced optimal transport regularization for imaging problems, *IEEE Transactions on Computational Imaging*, 6:1219–1232, 2020.
 - [52] Z. H. Ma, X. Wei, X. P. Hong, H. Lin, Y. F. Qiu and Y. H. Gong, Learning to count via unbalanced optimal transport, In *Proceedings of the AAAI Conference on Artificial Intelligence*, volume 35, 3, pages 2319–2327, 2021.
 - [53] Q. C. Le, D. Conte and M. Hidane, Unbalanced optimal transport in multi-camera tracking applications, In *Pattern Recognition, ICPR International Workshops and Challenges: Virtual Event*, January 10–15, 2021, *Proceedings, Part V*, pages 327–343, Springer, 2021.
 - [54] K. Fatras, T. Séjourné, R. Flamary and N. Courty, Unbalanced minibatch optimal transport; applications to domain adaptation, In *International Conference on Machine Learning*, pages 3186–3197, PMLR, 2021.
 - [55] K. Cao, Q. Y. Gong, Y. G. Hong and L. Wan, A unified computational framework for single-cell data integration with optimal transport, *Nature Communications*, 13(1):7419, 2022.
 - [56] X. Shen, W. Lam, S. M. Ma and H. D. Wang, Joint learning of text alignment and abstractive summarization for long documents via unbalanced optimal transport, *Natural Language Engineering*, pages 1–29, 2023.
 - [57] H. D. Plaen, P. D. Plaen, J. Suykens, M. Proesmans, T. Tuytelaars and L. V. Gool, Unbalanced optimal transport: A unified framework for object detection, In *Proceedings/CVPR, IEEE Computer Society Conference on Computer Vision and Pattern Recognition*, 2023.
 - [58] J. Dan, T. Jin, H. Chi, S. J. Dong and Y. X. Shen, Uncertainty-guided joint unbalanced optimal transport for unsupervised domain adaptation, *Neural Computing and Applications*, 35(7):5351–5367, 2023.
 - [59] H. Lavenant, S. Claici, E. Chien and J. Solomon, Dynamical optimal transport on discrete surfaces, *ACM Transactions on Graphics (TOG)*, 37(6):1–16, 2018.
 - [60] J. J. Yu, R. J. Lai, W. C. Li and S. Osher, Computational mean-field games on manifolds, *Journal of Computational Physics*, 484:112070, 2023.
 - [61] R. D. Neidinger, Introduction to automatic differentiation and matlab object-oriented programming, *SIAM review*, 52-3:545–563, 2010.
 - [62] D. P. Kingma and J. Ba, Adam: A method for stochastic optimization, *arXiv preprint*

- arXiv:1412.6980, 2014.
- [63] K. Xu, W. L. Sun, Z. Dong, Anisotropic spherical Gaussians, International Conference on Computer Graphics and Interactive Techniques, ACM, 2013.